Multiscale Reciprocal Space Mapping of Magnetite Mesocrystals

Aleksandra Chumakova,* Tristan Steegemans, Igor A. Baburin, Alexander Mistonov, Ilya S. Dubitskiy, Julian Schlotheuber, Felizitas Kirner, Sebastian Sturm, Axel Lubk, Knut Müller-Caspary, Ilona Wimmer, Mikhail Fonin, Elena V. Sturm,* and Alexeï Bosak*

Mesocrystals are a class of nanostructured material, where a multiple-length-scale structure is a prerequisite of many interesting phenomena. Resolving the mesocrystal structure is quite challenging due to their structuration on different length scales. The combination of small- and wide-angle X-ray scattering (SAXS and WAXS) techniques offers the possibility of non-destructively probing mesocrystalline structures simultaneously, over multiple length scales to reveal their microscopic structure. This work describes how high dynamical range of modern detectors sheds light on the weak features of scattering, significantly increasing the information content. The detailed analysis of X-ray diffraction (XRD) from the magnetite mesocrystals with different particle sizes and shapes is described, in tandem with electron microscopy. The revealed features provide valuable input to the models of mesocrystal growth and the choice of structural motif; the impact on magnetic properties is discussed.

1. Introduction

X-ray diffraction (XRD) is one of the most commonly used experimental techniques to characterize crystal structures. Mesocrystals—a form of nanostructured material, usually defined as a nanocrystal superstructure with a common crystallographic orientation—exhibit a multiple-length-scale structure. Mesocrystals can occur naturally in abiotic and biogenic minerals or can be synthesized artificially.[1]

Due to the crystallographic alignment of nanoparticles, mesocrystals exhibit a sharp wide-angle diffraction pattern. In addition, special types of mesocrystals (Type 1), which are characterized by a long-range packing order of (monodisperse) nanoparticles, additionally show single-crystal-like diffraction patterns in the small-angle scattering region.[2] Resolving the mesocrystal structure is quite challenging, due to their structuration on different length scales. Whereas the external morphology and structural features of mesocrystals are relatively simple to analyze by scanning electron microscopy (SEM) techniques, the analysis of the internal structure of 3D mesocrystals via the combination of scanning and transmission electron microscopy (TEM) requires time-consuming and difficult sample preparation (for example by focused ion beam milling). The combination of small- and wide-angle X-ray scattering (SAXS and WAXS) techniques offers the possibility to non-destructively probe mesocrystalline structures

A. Chumakova, F. Kirner, A. Bosak
European Synchrotron Radiation Facility
71 Avenue des Martyrs, Grenoble 38000, France
E-mail: aleksandra.chumakova@esrf.fr; alexei.bossak@esrf.fr

A. Chumakova
Outstation at Heinz Maier-Leibnitz Zentrum (MLZ)
Institute of Crystallography (IfK)
RWTH Aachen University
Lichtenbergstrasse 1, 85747 Garching, Germany

T. Steegemans, I. S. Dubitskiy, J. Schlotheuber
Julian Schlotheuber and Elena V. Sturm
Department of Chemistry
University of Konstanz
Universitaetsstraße 10, 78457 Konstanz, Germany

I. A. Baburin
Department of Chemistry
TU Dresden
Bergstraße 66b, 01062 Dresden, Germany

A. Mistonov, I. Wimmer, M. Fonin
Department of Physics
University of Konstanz
Universitätsstraße 10, 78457 Konstanz, Germany

F. Kirner, E. V. Sturm
Department of Earth and Environmental Sciences
Section of Crystallography
Ludwig-Maximilians-Universität München (LMU)
Theresienstr. 41C, 80333 Munich, Germany
E-mail: Sturm.Elena@lmu.de

S. Sturm, A. Lubk
Leibniz Institute for Solid State and Materials Research (IFW) Dresden
Helmholtzstraße 20, 01069 Dresden, Germany

S. Sturm, K. Müller-Caspary
Fakultät für Chemie und Pharmazie – Physikalische Chemie
Ludwig-Maximilians-Universität München
Butenandtstr. 5-13, 81377 München, Germany

**ADVANCED
SCIENCE NEWS**
www.advancedsciencenews.com

**ADVANCED
MATERIALS**
www.advmat.de

simultaneously over multiple length scales to reveal their microscopic structure. The combination of X-ray scattering techniques with physical property analysis can reveal structure–property relationships in such natural and synthetic 3D materials. Fundamental understanding of the multiscale organization of mesocrystals is potentially beneficial for applications in various fields such as catalysis,[3] surface-enhanced Raman scattering, electrodes,[4] lithium-ion batteries,[5] and biomedicine.[6]

Magnetite nanoparticles have caught significant attention in the past few years, due to their tendency to self-assemble into superstructures that even on the mesoscopic scale exhibit superparamagnetic properties of the nanoparticles, in contrast to the ferrimagnetic behavior of bulk magnetite.[1c] The stoichiometric magnetite possesses the structure of an inverse spinel with an $Fd\overline{3}m$ space group.[7] If the size of a magnetite nanoparticle exceeds multiple Weiss domains, magnetic anisotropies of the bordering domains cancel each other out, rendering the net magnetization essentially zero at room temperature and zero field.[8] For particle dimensions smaller than a single Weiss domain, the particle is spontaneously magnetized.[9] It should be noted that the magnetic properties of individual magnetite nanoparticles can be furthermore very different from the bulk due to surface effects and internal defects, which in turn are related to the particle size, shape, crystallinity, and degree of oxidation.[10]

The magnetic properties of magnetite mesocrystals as a particular case of magnetic nanoparticle assemblies are determined by the interplay of magnetic properties of individual nanoparticles (e.g., magnetocrystalline anisotropy), and their mutual interactions being of exchange and dipole–dipole type.[11] Therefore, understanding both the external and internal structure of magnetite mesocrystals is crucial to specify the complex structure–magnetism relationship of the material.[12] Nearly perfect ordering of exchange decoupled magnetic nanoparticles into 3D lattices, as well as the alignment of their crystallographic axes, make these mesocrystals a unique playground for studying collective magnetic properties of interacting particles.[1c] The appearance of some emergent effects in the case of the almost perfectly ordered mesocrystals can be expected,[13] which motivates further research.

The well-established SAXS and WAXS techniques date back to 60 years ago in terms of theory,[14] and deliver quantitative structural data for simultaneous examinations at both the atomic and mesoscopic length scale.[15] Huge progress was achieved along with the introduction of dedicated synchrotron radiation sources, and low noise and high dynamic range detectors. SAXS and WAXS data are typically collected using different hardware, however, an outstanding advantage is gained here from the combination of SAXS and WAXS at small-angle and macromolecular crystallography beamlines at the ESRF: soft-matter beamlines ID02 and ID10,[16] high-energy beamline ID15A,[17] and a SAXS station of BM26.[18] At these beamlines, a high flux density and a hybrid pixel detector allow for the exploitation of a diffractometer originally designed for single crystals to study mesocrystals.

Here, we present a detailed structural characterization of magnetite nanoparticles and their mesocrystals, (self-assembled from dispersion using a gas phase diffusion technique[19]) performed by the combination of electron microscopy and small- and wide-angle synchrotron XRD simultaneously measured at ID28 ESRF beamline.

2. Results and Discussion

In this work, we present the data obtained for magnetite nanocrystals with different sizes and degrees of cube truncation. Below, we define three nanoparticle batches chosen as representatives—A, B, and C—with increasing degrees of cube truncation (**Figure 1**). The whole range of studied samples produces three classes of structures—trigonal, base-centered monoclinic, and body-centered tetragonal (bct).

Typical scanning electron microscopy images of mesocrystals are shown in the left column of **Figure 2**. From the TEM data, it is known[12] that a lower degree of truncation promotes trigonal packing, and a high degree of truncation is a prerequisite for the formation of the bct structure. The prolate rhombohedral shape in sample A indicates trigonal symmetry. The same type of crystals is found in sample B, coexisting with an oblate (pseudo)rhombohedral shape. Truncated pyramids in sample C
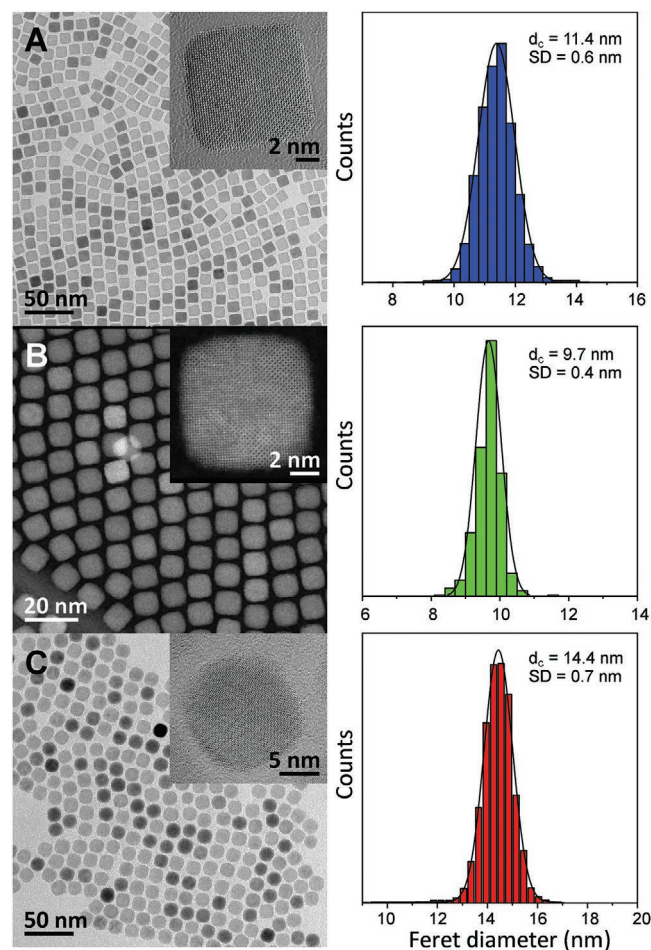

Figure 1. (Left) TEM (batch A and C) and STEM (batch B) images of monolayers of nanoparticles. High-resolution images of nanoparticles oriented along the [001] axis are shown in insets. (Right) Nanoparticle size distributions (i.e., Feret diameter of inorganic core—d_c, standard deviation—SD) as evaluated from microscopy images.
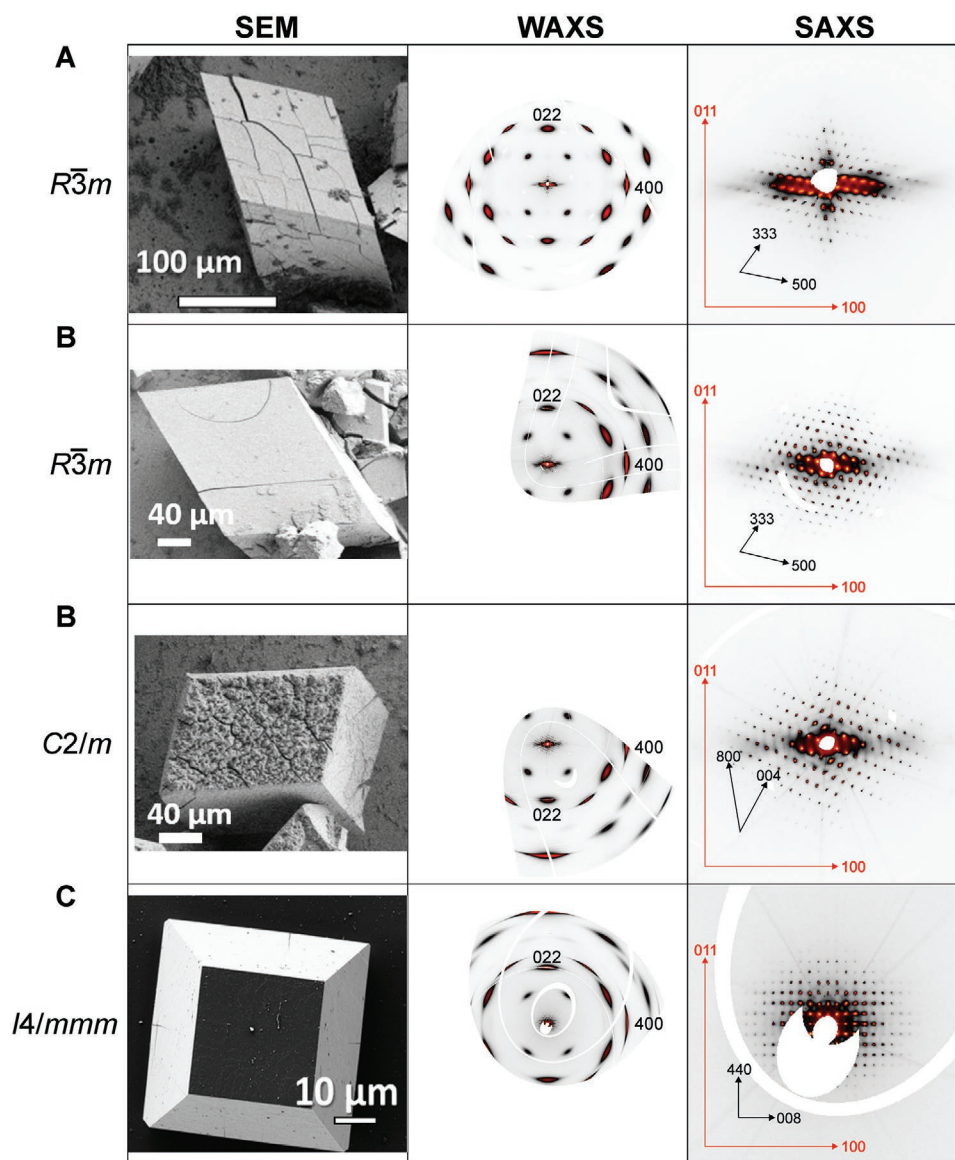
Figure 2. SEM images illustrating the morphology of mesocrystals (left column) related to WAXS (middle column) and SAXS (right column) high symmetry reconstructed planes. The red arrows denote reciprocal lattice translations of magnetite, the black arrows denote reciprocal lattice translations of the mesocrystalline packing.

serve as an indicator of an orthogonal cell. Monodomain mesocrystals can simply be recognized by their finished and uninterrupted structure.

Typical wide-field reconstructions of high-symmetry magnetite planes are shown in the middle column of Figure 2; close-ups of the small-angle part are shown in the right panels. From here on out, a combined linear-logarithmic scale is employed as it is conveniently implemented in the Albula software (Dectris). The small-angle scattering region (see Figure S1, Supporting Information for the details) is dominated by the diffraction from the large-period mesocrystalline arrangement. It is worth noting that more than 10 diffraction orders can be seen without any appreciable angular spread, indicating a remarkable perfection of the packing for large mesocrystals containing 10^{10} to 10^{12} particles. In combination with WAXS,

(Figure 2) precise orientational relationships can be established. For the reasons described below, full mapping of the reciprocal space must be preferred to the collection of diffraction in the selected zones, as frequently practiced in SAXS studies.

The summary of the translational symmetry is given in **Table 1**. It is worth underlining that monoclinic cell, not reported before, is metrically close to the oblate rhombohedral structure with angles ranging from 106° to 109° and, in turn, to the body-centered cubic structure (see Table S1 and Figure S2, Supporting Information for the details). Rhombohedral and tetragonal structures are rigidly attached to the cubic basis of spinel, while for monoclinic axis only twofold axis is aligned with spinel high symmetry direction; pseudo-threefold axis of P-1 cell is rotated by ≈8° in respect to 111 cubic direction. This geometry remains fixed for all the studied crystals of the batch.

**ADVANCED
SCIENCE NEWS**

www.advancedsciencenews.com

**ADVANCED
MATERIALS**

www.advmat.de

Table 1. Translational symmetry and orientational relationships in magnetite mesocrystals. Index S denotes the cubic spinel cell of magnetite.

Sample	Space group	Lattice parameters	Orientation
A	R-3m	$a = 127.2$ Å $\alpha = 70.3°$ $V = 1765$ nm³	<1–10>‖<1–10>$_S$ <111>‖<111>$_S$
B	R-3m	$a = 131.5$ Å $\alpha = 64.0°$ $V = 1750$ nm³	<1–10>‖<1–10>$_S$ <111>‖<111>$_S$
B	C2/m	$a = 216.2$ Å; $b = 208.6$ Å; $c = 129.0$ Å $\beta = 142.3°$ $V = 3558$ nm³	<010>‖<110>$_S$
C	I 4/mmm	$a = 154.7$ Å; $c = 248.7$ Å $V = 5930$ nm³	<100>‖<100>$_S$ <001>‖<001>$_S$

The absolute values of azimuthal widths of mesostructural peaks cannot be quantified for our data, as apparently all the mesostructural peaks we observed have the width of the order of detector pixel. We can only constrain the upper limit, which is not higher than 1 degree. This narrow distribution can be compared to much broader orientation distribution function (ODF) of magnetite itself. The shape of the ODF changes significantly with the degree of truncation (Figures S3 and S4, Supporting Information), while single particle orientation type is retained for all the samples. For the lowest truncation degree (A) the angular spread is close to 5° FWHM (4.7° to 5.6° in orthogonal directions), nearly doubles for intermediate truncation (B), and raises to 12.3° FWHM around in-plane directions for the sample C. Such a feature is quite natural considering a significant looser packing, and the absence of large face-to-face contacts in the bct structure as compared to a trigonal one.

As can be seen, the small-angle diffraction pattern is decorated by diffuse scattering, but its modeling necessitates a better momentum resolution. Magnetite spots are subject to broadening due to both the effect of particle size and the angular spread; the effect is illustrated in **Figure 3**. The above contributions have to be analyzed separately. The most remarkable features are the interference ripples around spinel Bragg nodes $h+k = 4n$, $h+l = 4n$, and $k+l = 4n$, i.e., 400, 222, and 440, coinciding with the allowed reflections in oxygen close-packed lattice. Those ripples propagate along the reciprocal lattice vector. For the remaining spots, the peak profile is featureless and significantly broader and should be related to the antiphase boundaries with translation vector [1/4 1/4 0] (see Appendix II), similar to previous TEM observations in magnetite[21] and powder diffraction in γFe$_2$O$_3$.[22] Magnetization can thus be significantly affected and the effective size of the magnetic domains can be reduced compared to the nanoparticle size.

Note that in the case of mesocrystals, the SAXS and WAXS regions cannot be fully separated since high orders of small-angle diffraction can merge with the low orders of diffraction from the atomic arrangement, as visible for the trigonal mesocrystal in Figure 3. The family of spots, generally forbidden in stoichiometric magnetite, is apparent and likely corresponds to the excess of oxygen, which is known to destroy
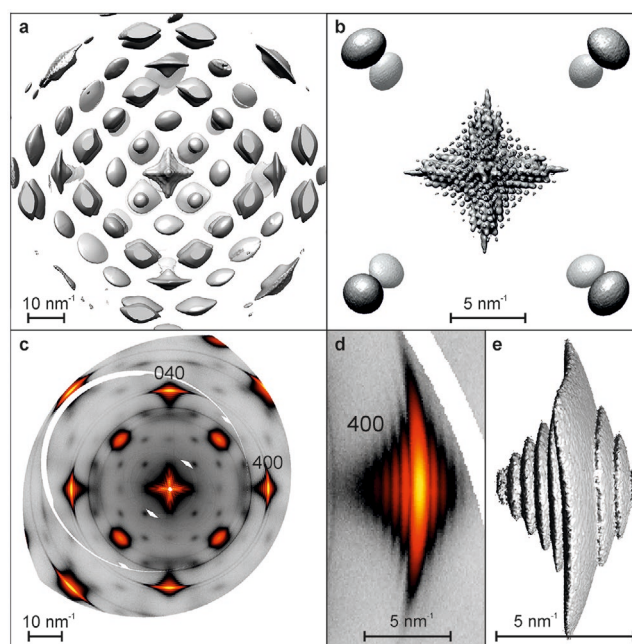

Figure 3. Reciprocal space maps of mesocrystal sample A: a,b,e) constant intensity surfaces and c,d) 2D *hk*0 intensity maps for selected areas with different magnification. Laue symmetry operations were applied to the maps in order to minimize the empty volume due to the detector gaps.

both F and d symmetry elements.[23] We found no indications in favor of the formation of secondary phases.

WAXS data, beyond some momentum transfer, can be considered as an incoherent sum of individual diffraction patterns of nanoparticles. A fully quantitative treatment of the interference pattern is hardly possible. However, the positions of minima/maxima, as well as the decay of oscillations, can be treated within a simple model, where the intensity approximated as

$$I \sim \mathrm{sinc}^2(aD) \otimes \exp\left(\frac{-D^2}{2\sigma^2}\right) \tag{1}$$

give an estimate of the distance D between two parallel facets of particle and the estimate of its spread σ (**Figure 4**). The analysis of interference ripples in the proximity of 400, 440, and 222 spots give an envelope of cuboctahedral shape, summarized in **Table 2** and illustrated by **Figure 5**. A proper error estimate is not possible since a proper fitting procedure could not be applied. In particular, it is hard to properly quantify the peak asymmetry, which is especially pronounced for trigonal crystals (see Figures 3 and 4). Qualitatively, the asymmetry is linked to the so-called "size effect", known in diffuse scattering,[24] which is reduced here to the trivial fact that is larger than average particles (and thus stronger scatterers) are pushed away from each other.

The case of sample B is particularly interesting from the crystallogenic point of view. TEM and scanning TEM (STEM) observations (Figure 1; Figure S5 and S6, Supporting Information) indicate a *c2mm* monolayer packing for the small-to-modest truncation, the subsequent choice of growth mode is apparently selected by the positioning of the second layer. If the second layer is shifted along the long axis, a prolate
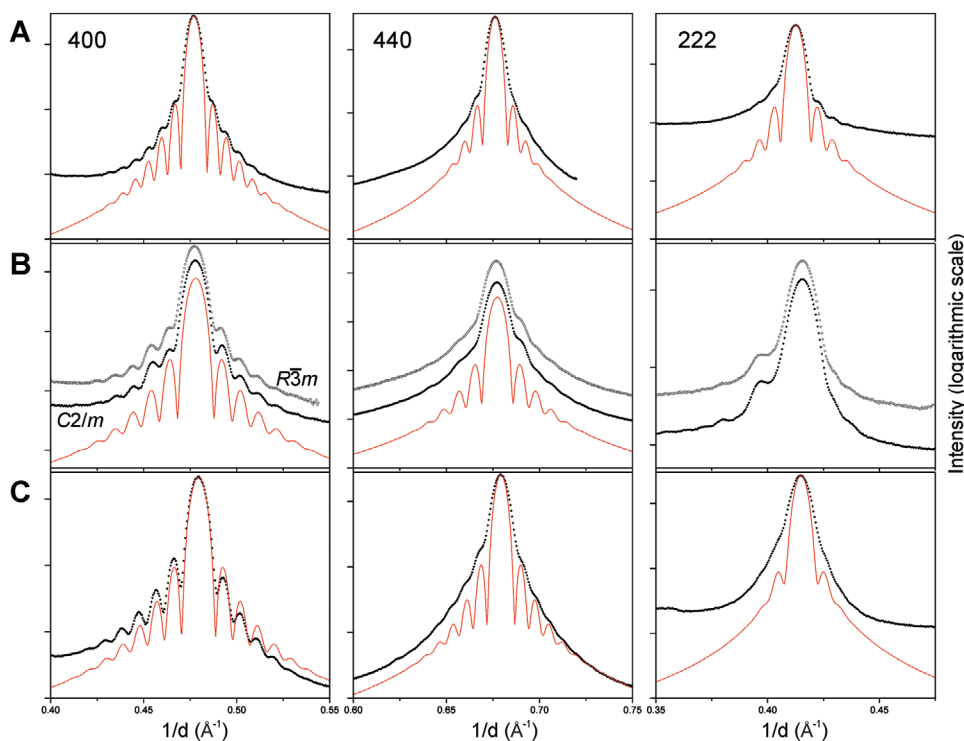
**ADVANCED
SCIENCE NEWS**

www.advancedsciencenews.com

**ADVANCED
MATERIALS**

www.advmat.de

Figure 4. The intensity profiles in the radial direction across 400, 440, and 222 for three sets of nanoparticles (A,B,C). The symbols indicate the experimental data, red continuous lines correspond to the modeling by Equation (1). Note that for set (B), the profiles for trigonal and monoclinic structures are essentially identical; the profile for the 222 spot cannot be treated by our model. Profiles are shifted along the vertical axis for better visibility; vertical axis ticks correspond to factor 10 step.

parallelepiped forms, and by the emerging tilt of nanoparticles a threefold axis is built. If the second layer is shifted along the short axis, an oblate parallelepiped forms but the tilt of nanoparticles stays at a general value not increasing the symmetry to threefold (Figure S7, Supporting Information).

The analysis of the contacts between the nanoparticles appears rather instructive, as far as we consider only short-range interaction, essentially limited by the surfactant layer thickness (see Appendix I). The simplest case is, obviously, $I4/mmm$ packing, where {100}-face contacts are the only ones affecting the spacing in the a–b plane, and only {111}-face contacts are responsible for the interlayer interaction and thus for the c spacing. The ratio c/a is calculated in such a way from the values in Table II with a contact distance of $\Delta = 1.3$ nm which is 1.643, to be compared to the experimental number 1.608. The primitive cubic packing of coated cubes, truncated or not, is unstable with respect to shear as the returning force is negligible in the surfactant layer. As we see, the structure can relax in different ways as a function of truncation. For the rhombohedral distortion cooperative sliding along the {100}

faces is accompanied by the emergence of close contacts for every other {110} face. Such a constraint limits the rhombohedral distortion. The estimated angles for samples A ($\Delta \approx 1.5$ nm) and B ($\Delta = 2.5$ nm) are equal to 71.9° and 66.1°, within 2° from the experiment. It is worth noting that even if the rhombohedral angle will be accidentally equal to 60°, the structure will not become face-centered cubic, because the $Fm\overline{3}m$ symmetry will not be compatible with the particle orientation (Figure S8, Supporting Information). The monoclinic packing requires five variables for the description (three lattice dimensions, one monoclinic angle, and the particle rotation around the 2-fold axis), while the independent contact constraints are limited to four: two inequivalent {100} contacts, one {110} and one {111} contact. Thus, the maximization of contact surface becomes a counterweight. For known particle rotation angles, the corresponding geometric estimates allowed us to constrain the truncation along {111}, resulting in a 11.5 nm value.

To reveal the effect of nanoparticle ordering and orientation on the magnetic properties of assemblies, it is essential to analyze the magnetic properties of disordered nanoparticle

Table 2. The geometry of cuboctahedral particles (d—distance between parallel faces) as derived from the diffraction data.

	A		B		C	
	d [nm]	FWHM [nm]	d [nm]	FWHM [nm]	d [nm]	FWHM [nm]
100	11.0	1.5	10.3	1.5	14.2	2
110	13.5	2.5	12.0	2.5	15.0	3.5
111	14.0	5.0	[11.5]	-	15.0	3.5

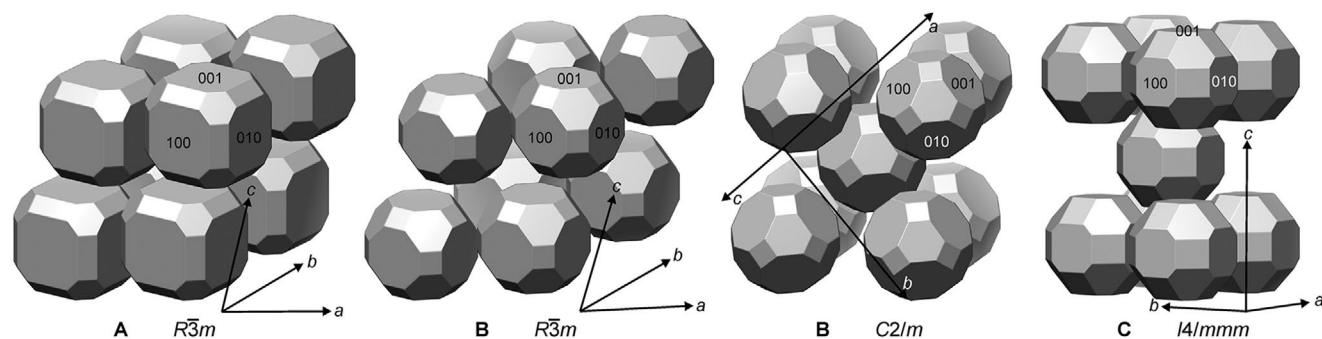**Figure 5.** Packing of nanoparticles for trigonal, monoclinic, and tetragonal structures. For B, truncation along <111> is introduced following the constraints described in the text to avoid the particles being in too close proximity. One family of facets is labeled by three orthogonal directions of magnetite; vectors are given in the cell definitions of Table 1.

powder, isolated nanoparticles in a solid matrix (i.e., isolated system: nanoparticles in solid docosane), and mesocrystals assembled from the same magnetic nanoparticles. The magnetization measurements showed, as expected, superparamagnetic behavior for the nanoparticle batches A, B, and C demonstrated by the hysteresis measured at 4 K (**Figure 6** and Figure S11, Supporting Information). In order to obtain the blocking-temperature distribution, the first temperature derivative of the difference between zero-field cooling (ZFC) and field cooling (FC) was taken.[25] Original ZFC-FC curves are presented in Figures S9–S11 (Supporting Information). For the batch B nanoparticles ($d_c = 9.7$ nm) we obtain $T_B = 84$ K. Increasing nanoparticle size to 11.4 nm (batch A) and to 14.4 nm (batch

C) leads to a further increase of T_B to 107 K and 132 K, respectively. The observed increase in T_B with increasing particle size is in line with the expected trend given by $T_B \simeq K_a V$, with K_a being the effective anisotropy constant and V particle volume. However, we note that K_a actually does not remain constant assuming that K_a is proportional to the coercive field H_C. In particular, the difference between batch A and batch C particles can be attributed not only to the size dependence of K_a but also to the shape dependence, as reported in size,[26] where octahedral-shaped nanoparticles showed higher anisotropy than cube-shaped ones at comparable size.

We now investigate the impact of ordered arrangement of particles on the magnetic properties of the system. For this
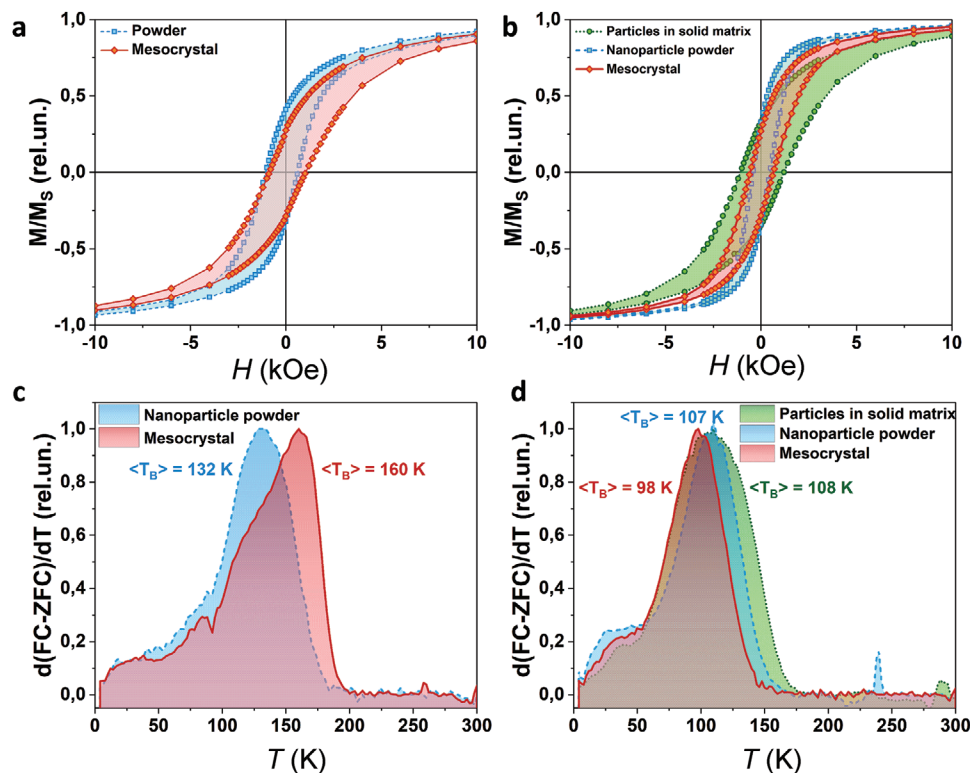

Figure 6. a–d) Magnetization curves measured at 4 K and the first derivatives of the FC-ZFC difference obtained for the batch C (a,c) and batch A (b,d) isolated nanoparticles in a solid matrix, powder, and mesocrystal.

purpose, we investigate batch A and batch B nanoparticles, which first show the largest difference in shape and second the largest difference in K_a. In Figure 6a one can see that a change in the arrangement of the batch C nanoparticles from randomly oriented nanoparticle powder to an ordered mesocrystal slightly affects the remanence (0.36 MS to 0.29 MS) and coercivity (852 to 951 Oe) at low temperature, as well as significant shifts the average blocking temperature—from 132 to 160 K (Figure 6c). At the same time, for batch A (Figure 6b,d) we found that the particle arrangement only influences coercivity (1140 Oe for particles in a solid matrix, 440 Oe for nanoparticle powder, and 610 Oe for mesocrystal), while the blocking temperature remains about 100 K for all three considered compositions. In order to discuss the variation of T_B upon ordering, we imply that dipolar interactions represent the main coupling mechanism between the particles in the systems under study. Obviously, the interparticle interaction depends on the distance between the nanoparticles.[27] In case of batch C the assembly into the mesocrystal results in a smaller effective distance between the particles, higher dipolar interaction, and thus increased T_B. This effect is however absent for the batch A nanoparticles, which can be related to a higher surface spin disorder as can be deduced from the exchange bias observed in the magnetization measurements. For the batch C nanoparticles with high magnetic anisotropy constituting a mesocrystal, we expect less magnetic disorder in terms of the spatial orientation of the magnetic easy axis of individual nanoparticles, which would again lead to a dipolar energy and consequently higher T_B in the ordered crystal as compared to the powder sample. Further experiments, including real space magnetic, imaging is necessary in order to obtain detailed information on the magnetic configuration of the mesocrystals at low temperatures.

3. Conclusion

An experiment using simultaneous or quasi-simultaneous SAXS–WAXS data collection employing the PILATUS-based ID28 ESRF diffractometer on self-assembled magnetite mesocrystals is presented, complementing the electron microscopy and magnetization measurement data. A high dynamical range availability sheds light on the weak features of scattering, significantly increasing the information content. For mesocrystals of different nanoparticle sizes and shapes and, correspondingly, different packing modes, the 3D periodicity was extracted. Furthermore, for the constituent particles, the orientation distribution function and shape and size distributions helped to build an average idealized model of magnetite mesocrystals. Unexpected polymorphism—coexistence of trigonal and monoclinic crystals— was found for the mesocrystals self-assembled from modestly truncated cubes. Also, a semi-quantitative explanation of the packing details based on the analysis of the particle contact distances was given.

It was shown that size–shape parameters of the considered nanoparticles along with their arrangement, strongly affect magnetic properties of solid mesocrystalline materials. Whereas, large and highly truncated particles have higher blocking temperatures that are significantly shifted to higher temperatures when self-assembled into mesocrystals, small

particles with a low degree of truncation have similar blocking temperatures for all three considered arrangements. Even though a detailed analysis of the physical aspects that play a role in the magnetic behavior of ordered assemblies is beyond the scope of this paper, it is worth noting that the possibility to study mesocrystals at different length scales is of great importance for constructing the structure–property relationship of such systems.

4. Experimental Section

Nanoparticle Synthesis: The synthesis of magnetite nanocubes was conducted via the thermal decomposition of an iron(III)-oleate complex.[12] First, 9.08 g (10 mmol) of iron(III)oleate, 0.436 g (1.43 mmol) of sodium oleate, 0.453 g (1.43 mmol) of oleic acid (Tokyo Chemical Industry, 99%), and 50 mL of 1-octadecene (Sigma-Aldrich, 90%) were added together in a 250 mL three-necked round bottom flask equipped with a magnetic stir bar, in situ temperature sensor, and a Dimroth condenser.

The mixture was heated up to 60 °C and degassed for 60 min by flushing with nitrogen three times. After degassing, the mixture was heated up to the reflux temperature of 320 °C using a heating ramp of 3 °C min^{-1} and kept at 320 °C for 30 min before being cooled down to room temperature, resulting in a black dispersion. Finally, the dispersion was purified by centrifugation (Hettich Universal 320) using toluene for redispersion and ethanol for sedimentation. Lastly, the product was dispersed in tetrahydrofuran (THF, VWR Chemicals, 99%) containing 3 µL mL^{-1} oleic acid.

Mesocrystal Synthesis: The self-assembly of magnetite mesocrystals was performed using the gas phase diffusion technique previously optimized for this system.[19] A sketch of an experimental setup can be found in Figure S12 (Supporting Information). The mesocrystals were prepared by adding 900 µL of purified magnetite nanocubes dispersed in THF or cyclohexane containing oleic acid (3 µL mL^{-1}) to a 1 mL flat bottom vial equipped with a double-sided polished Si wafer. This vial was placed in a larger screw-on cap vial containing 1 mL of 50:50 THF/EtOH or cyclohexane/EtOH solution (corresponding to the nanoparticle dispersion solvent) as an antisolvent. The screw-on cap was subsequently loosely closed and for storage during the self-assembly process, the screw-on cap vial was placed in a closed desiccator with 5 mL THF/EtOH or cyclohexane/EtOH mixture and stored out of direct sunlight under room temperature until the self-assembly process was completed. The combination of stacked vessels was experimentally improved for a fast diffusion process (5–7 days) with good mesocrystal yield. The finished self-assembly was indicated by the discoloration of the nanoparticle dispersion in the inner vial from black to light-transparent brown. The Si wafer containing the mesocrystals could be subsequently removed for further investigations. However, to improve the mesocrystal quality, a recrystallization process was carried out as previously published.[20] The supernatant in the inner vial was removed using a syringe, and the assembled mesocrystals were subsequently redispersed (in the same vial/setup) in 600 µL of THF with 3 µL mL^{-1} oleic acid, and the self-assembly process recurred. Recrystallization could be carried out as much as four times to narrow the particle size distribution and lead to high-quality mesocrystals.

Electron Microscopy: SEM images of mesocrystals were collected using a Zeiss Gemini 500. TEM images of nanoparticles and 2D assemblies were recorded by means of a double aberration-corrected FEI Titan[3] transmission electron microscope, operated at 300 kV acceleration voltage. Scanning TEM images were obtained on a probe-corrected FEI Themis at an acceleration voltage of 300 kV. The TEM and STEM images were analyzed with the DigitalMicrograph Gatan Microscopy Suite 3 software (Gatan Inc., ver. 3.41.2938.1). The core diameter of the nanocrystal batches were evaluated from TEM images by using the Fiji software[28] with the Trainable WEKA Segmentation plugin.[29] The distribution histograms were fitted using a Gaussian function.

**ADVANCED
SCIENCE NEWS**

www.advancedsciencenews.com

**ADVANCED
MATERIALS**

www.advmat.de

Diffraction Data Collection: The ambient temperature XRD data were collected at ID28 diffractometer[30] at the wavelengths λ = 0.697 Å and λ = 0.980 Å; the typical beam size was about 40 μm FWHM. Data were recorded by a single-photon-counting PILATUS3 1 M detector, positioned at 244 or 414 mm away from the sample, in shutterless mode over a rotation of 360° with 0.25° step. The experimental momentum resolution for the given sample size, beam size, and divergence was essentially dominated by the pixel size. The experimental geometry and the orientation matrix were refined using CrysAlis^Pro software;[31] locally developed software was used for high-resolution 2D and 3D reconstructions, and for the selected area and selected volume intensity integration.

Magnetic Measurements: Superconductive quantum interference device (SQUID) measurements on unordered powder, nanoparticles in matrices, and mesocrystals were performed using a Quantum Design MPMS-XL5 magnetometer. Remagnetization curves were measured at 4 and 300 K, while the external magnetic field was in the range of -35 to 35 kOe. ZFC-FC measurements were performed at 20 Oe. Unordered magnetite nanoparticle powder for SQUID analysis was prepared by the addition of EtOH to the nanoparticle solution, and subsequent centrifugation at 3000 rpm for 15 min. The supernatant was decanted, and the remaining nanoparticle sediment was dried overnight in a vacuum at 40 °C. Particle matrices for SQUID analysis were prepared by the redispersion of unordered magnetite powder into docosane, (T_m = 42–45 °C) using a heating bath to keep the docosane liquid during redispersion. The particle-docosane dispersion was transferred to a 0.5 mL gelatine capsule, which was immediately cooled in liquid nitrogen yielding a solid particle matrix.

Supporting Information

Supporting Information is available from the Wiley Online Library or from the author.

Acknowledgements

Conflict of Interest

The authors declare no conflict of interest.

Data Availability Statement

The data that support the findings of this study are available from the corresponding author upon reasonable request.

Keywords

[1] a) H. Cölfen, M. Antonietti, *Mesocrystals and Nonclassical Crystallization*, Wiley, Chichester, UK 2008; b) E. V. Sturm, H. Cölfen, *Crystals* 2017, *7*, 207; c) E. V. Sturm, H. Cölfen, *Chem. Soc. Rev.* 2016, *45*, 5821.

[2] L. Bergström, E. V. Sturm, G. Salazar-Alvarez, H. Cölfen, *Acc. Chem. Res.* 2015, *48*, 1391.

[3] a) J. Fang, B. Ding, H. Gleiter, *Chem. Soc. Rev.* 2011, *40*, 5347; b) T. Tachikawa, T. Majima, *NPG Asia Mater.* 2014, *6*, 100.

[4] L. Bahrig, S. G. Hickey, A. Eychmüller, *CrystEngComm* 2014, *16*, 9408.

[5] E. Uchaker, G. Cao, *Nano Today* 2014, *9*, 499.

[6] L. Zhou, P. O'Brien, *J. Phys. Chem. Lett.* 2012, *3*, 620.

[7] a) M. E. Fleet, *Acta Crystallogr B* 1981, *37*, 917; b) R. M. Cornell, U. Schwertmann, *The Iron Oxides: Structure, Properties, Reactions, Occurrences and Uses*, Wiley-VCH, Weinheim, Germany 2003.

[8] C. Kittel, P. McEuen, *Introduction to Solid State Physics*, John Wiley & Sons, Hoboken, NJ, USA 2018.

[9] J. Frenkel, J. Doefman, *Nature* 1930, *126*, 274.

[10] a) R. Yanes, O. Chubykalo-Fesenko, H. Kachkachi, D. A. Garanin, R. Evans, R. W. Chantrell, *Phys. Rev. B* 2007, *76*, 064416; b) V. Russier, C. de-Montferrand, Y. Lalatonne, L. Motte, *J. Appl. Phys.* 2013, *114*, 143904; c) K. L. Pisane, S. Singh, M. S. Seehra, *Appl. Phys. Lett.* 2017, *110*, 222409; d) W. Baaziz, B. P. Pichon, C. Lefevre, C. Ulhaq-Bouillet, J.-M. Greneche, M. Toumi, T. Mhiri, S. Bégin-Colin, *J. Phys. Chem. C* 2013, *117*, 11436; e) A. Mitra, J. Mohapatra, S. S. Meena, C. V. Tomy, M. Aslam, *J. Phys. Chem. C* 2014, *118*, 19356; f) B. Gross, S. Philipp, E. Josten, J. Leliaert, E. Wetterskog, L. Bergström, M. Poggio, *Phys. Rev. B* 2021, *103*, 014402.

[11] a) M. Blanco-Mantecón, K. O'Grady, *J. Magn. Magn. Mater.* 2006, *296*, 124; b) G. Barrera, P. Allia, P. Tiberto, *Nanoscale* 2021, *13*, 4103.

[12] J. Brunner, I. A. Baburin, S. Sturm, K. Kvashnina, A. Rossberg, T. Pietsch, S. Andreev, E. Sturm, H. Cölfen, *Adv. Mater. Interfaces* 2017, *4*, 1600431.

[13] a) I. Lisiecki, D. Parker, C. Salzemann, M. P. Pileni, *Chem. Mater.* 2007, *19*, 4030; b) J. Chen, A. Dong, J. Cai, X. Ye, Y. Kang, J. M. Kikkawa, C. B. Murray, *Nano Lett.* 2010, *10*, 5103.

[14] A. Guinier, G. Fournet, *Small-Angle Scattering of X-rays*, John Wiley & Sons, New York 1955.

[15] a) B. Gurun, Y. S. Thio, D. G. Bucknall, *Rev. Sci. Instrum.* 2009, *80*, 123906; b) J. Baldrian, M. Steinhart, P. Vlček, M. Horký, P. Laggner, H. Amenitsch, S. Bernstorff, *J. Macromol. Sci., Part B: Phys.* 2002, *41*, 1023; c) D. Pontoni, J. Bolze, N. Dingenouts, T. Narayanan, M. Ballauff, *J. Phys. Chem. B* 2003, *107*, 5123.

[16] a) T. Beuvier, E. A. C. Panduro, P. Kwaśniewski, S. Marre, C. Lecoutre, Y. Garrabos, C. Aymonier, B. Calvignac, A. Gibaud, *Lab Chip* 2015, *15*, 2002; b) T. Beuvier, I. Probert, L. Beaufort, B. Suchéras-Marx, Y. Chushkin, F. Zontone, A. Gibaud, *Nat. Commun.* 2019, *10*, 751.

[17] J. Daniels, *J. Appl. Crystallogr.* 2008, *41*, 1109.

[18] S. Nikitenko, A. M. Beale, A. M. J. van der Eerden, S. D. M. Jacques, O. Leynaud, M. G. O'Brien, D. Detollenaere, R. Kaptein, B. M. Weckhuysen, W. Bras, *J. Synchrotron Radiat.* 2008, *15*, 632.

[19] a) J. Schlotheuber né Brunner, B. Maier, S. L. J. Thomä, F. Kirner, I. A. Baburin, D. Lapkin, R. Rosenberg, S. Sturm, D. Assalauova, J. Carnis, Y. Y. Kim, Z. Ren, F. Westermeier, S. Theiss, H. Borrmann, S. Polarz, A. Eychmüller, A. Lubk, I. A. Vartanyants, H. Cölfen, M. Zobel, E. V. Sturm, *Chem. Mater.* 2021, *33*, 9119. b) J. J. Schlotheuber née Brunner, B. Maier, F. Kirner, S. Sturm, H. Cölfen, E. V. Sturm, *Cryst. Growth Des.* 2021, *21*, 5490.

[20] J. Brunner, B. Maier, R. Rosenberg, S. Sturm, H. Cölfen, E. V. Sturm, *Chem. - Eur. J.* 2020, *26*,15242.

[21] Z. Nedelkoski, D. Kepaptsoglou, L. Lari, T. Wen, R. A. Booth, S. D. Oberdick, P. L. Galindo, Q. M. Ramasse, R. F. L. Evans, S. Majetich, V. K. Lazarov, *Sci. Rep.* 2017, *7*, 45997.

[22] T. Kohler, A. Feoktystov, O. Petracic, N. Nandakumaran, A. Cervellino, T. Bruckel, *J. Appl. Crystallogr.* 2021, *54*, 1719.

[23] V. Chlan, J. Żukrowski, A. Bosak, Z. Kąkol, A. Kozłowski, Z. Tarnawski, R. Řezníček, H. Štěpánková, P. Novák, I. Biało, J. M. Honig, *Phys. Rev. B* **2018**, *98*, 125138.

[24] T. Welberry, *J. Appl. Cryst.* **1986**, *19*, 382.

[25] I. J. Bruvera, P. M. Zélis, M. P. Calatayud, G. F. Goya, F. H. Sánchez, *J. Appl. Phys.* **2015**, *118*, 184304.

[26] H. Mamiya, H. Fukumoto, J. L. C. Huaman, K. Suzuki, H. Miyamura, J. Balachandran, *ACS Nano* **2020**, *14*, 8421.

[27] J. Dai, J.-Q. Wang, C. Sangregorio, J. Fang, E. Carpenter, J. Tang, *J. Appl. Phys.* **2000**, *87*, 7397.

[28] J. Schindelin, I. Arganda-Carreras, E. Frise, V. Kaynig, M. Longair, T. Pietzsch, S. Preibisch, C. Rueden, S. Saalfeld, B. Schmid, J.-Y. Tinevez, D. J. White, V. Hartenstein, K. Eliceiri, P. Tomancak, A. Cardona, *Nat. Methods* **2012**, *9*, 676.

[29] I. Arganda-Carreras, V. Kaynig, C. Rueden, K. W. Eliceiri, J. Schindelin, A. Cardona, H. S. Seung, *Bioinformatics* **2017**, *33*, 2424.

[30] CrysAlisPRO, Rigaku Oxford Diffraction.

[31] A. Girard, T. Nguyen-Thanh, S. M. Souliou, M. Stekiel, W. Morgenroth, L. Paolasini, A. Minelli, D. Gambetti, B. Winkler, A. Bosak, *J. Synchrotron Radiat.* **2019**, *26*, 272.

2207130 (9 of 9)